Applied Physics Reviews ARTICLE pubs.aip.org/aip/are

On-chip mid-infrared spectroscopy without mid-infrared photons

Cite as: Appl. Phys. Rev. **13**, 011404 (2026); doi: 10.1063/5.0291359
Submitted: 17 July 2025 · Accepted: 28 November 2025 ·
Published Online: 5 January 2026

Boyi Xue,[1] Renhong Gao,[2] Yicheng Zhu,[1] Hengzhe Yan,[1] Jiankun Hou,[1] Xianfeng Chen,[3] Ya Cheng,[2,4,a)] Jintian Lin,[4,a)] Li Ge,[5,a)] and Wenjie Wan[1,2,3,a)]

AFFILIATIONS

[1]State Key Laboratory of Photonics and Communications, University of Michigan-Shanghai Jiao Tong University Joint Institute, Shanghai Jiao Tong University, Shanghai 200240, China
[2]State Key Laboratory of Precision Spectroscopy, East China Normal University, Shanghai, China
[3]Department of Physics and Astronomy, Shanghai Jiao Tong University, Shanghai 200240, China
[4]State Key Laboratory of High Field Laser Physics and CAS Center for Excellence in Ultra-Intense Laser Science, Shanghai Institute of Optics and Fine Mechanics (SIOM), Chinese Academy of Sciences (CAS), Shanghai 201800, China
[5]Department of Physics and Astronomy, College of Staten Island, The City University of New York, New York 10314, USA

Note: This paper is part of the APR Special Topic on Quantum Sensing.
[a)]**Authors to whom correspondence should be addressed:** ycheng@phy.ecnu.edu.cn; jintianlin@siom.ac.cn; li.ge@csi.cuny.edu; and wenjie.wan@sjtu.edu.cn

ABSTRACT

Mid-infrared (mid-IR) spectra revealing the distinct "fingerprint" of molecules are of critical importance for both science and technology in chemistry, physics, materials science, and biology. Mid-IR sensing and spectroscopy provide unique and powerful tools for crucial applications in greenhouse gas monitoring, hazardous emission detection, and medical breath diagnosis. However, the low-photon energy characteristic of the mid-IR spectrum poses significant challenges for both mid-IR light sources and detectors, hindering their compact and cost-efficient applications in various areas. Here, we experimentally demonstrate mid-IR gas spectroscopy without mid-IR photons solely using convenient near-IR optical components. This is realized by generating photon pairs (i.e., a mid-IR photon and a near-IR one) through a spontaneous parametric downconversion in a microscale optical cavity. The generation rate of near-IR photons strongly relies on the absorption of the mid-IR photon due to their quantum correlation. Through interacting with evanescent fields around the microcavity, the absorptive mid-IR resonances of the surrounding gas greatly affect the detected near-IR photons without harassing any mid-IR photon. This scheme presents a cost-effective and compact solution for on-chip quantum gas spectroscopy without requiring expensive mid-IR lasers and detectors or lasers, thereby paving new avenues for applications in environmental monitoring/safety, healthcare, and agriculture.

I. INTRODUCTION

The mid-infrared (mid-IR) spectral region, spanning 2 to 20 μm, is crucial for its unique ability to provide "molecular fingerprints" of the fundamental vibrational modes of molecules. This makes mid-IR spectroscopy an invaluable tool for identifying molecular compositions non-intrusively across various states of matter for analytical chemistry, biomedicine, and environmental monitoring.[1–3] They can provide detailed insights into molecular structures of complex biological and chemical systems[4–7] and help diagnose medical conditions via exhaled gases.[8] Also, mid-IR spectroscopy benefits from atmospheric transparency windows, enabling sensitive environmental gas sensing for ensuring air quality, monitoring greenhouse gases, and detecting hazardous or toxic emissions in industrial environments.[3,9,10] Particularly, this technology is instrumental for satellite missions addressing climate change, such as NASA's Orbiting Carbon Observatory and JAXA's GOSAT,[11,12] which aim to quantify carbon dioxide (CO_2) emissions. For these various applications, it is urgent and critical to develop portable and chip-scale mid-IR sources and gas sensors.[3,13,14] However, the mid-IR region has posed significant challenges for photonics, primarily due to the intrinsic noise of detectors made from narrow-bandgap materials and the difficulty in realizing efficient light emitters.[15,16] The introduction of inter-subband devices such as quantum-well infrared

photodetectors and quantum cascade lasers has significantly enhanced the mid-IR capabilities.[17,18] However, scalable substrate growth[19] and integration with silicon CMOS chips[20] remain substantial hurdles for costly on-chip mid-IR device integration.[21]

Recently, a groundbreaking approach to quantum imaging and spectroscopy has emerged, surprisingly circumventing the need to detect signal photons.[22] This technique exploits quantum interference between signal and idler photons generated through two cascaded spontaneous parametric downconversion (SPDC) processes.[23–25] In the first SPDC, a signal-idler photon pair is created. The signal photon, carrying information from an object, can transfer this information to the idler through quantum interference in the second SPDC, eliminating the necessity of direct signal photon detection. Notably, this method does not require an additional light source for the signal, making it well-suited for mid-infrared sensing.[26] This technique has rapidly gained attention for its potential applications in refractometry,[27] optical coherence tomography,[28,29] and imaging.[22,30,31] However, its reliance on the precise relative phase between signal and idler photons propagating between the two nonlinear SPDC crystals presents a significant challenge for stability control and practical implementation.

In recent years, whispering-gallery mode (WGM) microcavity-based optical sensors have witnessed significant advances. These resonators are capable of confining light within microscale volumes while exhibiting ultrahigh-quality (Q) factors, making them a cornerstone platform for photonic sensing due to their dramatic enhancement of light–matter interactions.[32,33] The operational principle of WGM sensors involves monitoring perturbations to their resonant modes, such as resonance shifts,[34] splitting,[35] or broadening[36]—resulting from environmental variations or interactions between the evanescent field and target analytes. Early studies demonstrated the detection of nanoparticles and viruses by monitoring such resonant shifts,[37] and subsequent research has substantially expanded the capabilities of this platform. For instance, techniques such as cavity ring-up spectroscopy have improved the time resolution of these measurements to the nanosecond regime.[38] Further innovations—including plasmonic enhancement,[39] noise suppression,[40] spontaneous chiral symmetry breaking scheme[41] as well as the utilization of interface whispering-gallery modes[42]—have significantly lowered the detection limit, enabling the measurement of minute perturbations. Together, these advances highlight the versatility and promise of WGM sensors for a wide spectrum of applications, ranging from single-molecule-level nanoparticle detection[36,41,43,44] and label-free biological analysis[42,45,46] to medical diagnostics,[47] spectroscopy,[48,49] temperature monitoring,[50] and pressure sensing.[51] Owing to these merits, WGM microcavities constitute a highly promising platform for our gas spectroscopy experiments.

In this work, we demonstrate mid-IR gas spectroscopy without mid-IR photons through SPDC in an optical microcavity with convenient near-IR optical components. The cavity-enhanced SPDC simultaneously generates a near-IR signal photon and its mid-IR idler, and the corresponding generation rate highly depends on both photons' absorption through their quantum correlation. Through interacting with evanescent fields around the microcavity, the absorptive resonances of gas in the mid-IR greatly affect such SPDC and its near-IR photons, which later can be detected for the related mid-IR resonances. Mid-IR photons are not necessarily generated or detected during the whole process. Compared to other compact, on-chip sensing approaches,[3,9,13,14,52] our approach offers distinct advantages. By leveraging quantum correlations, it eliminates the need for costly and complex mid-infrared light sources or detectors. Furthermore, the use of resonance-enhanced optical modes enables a significantly longer effective optical path than what is achievable with integrated waveguides alone.[9,52] Finally, our scheme requires only a single SPDC source, in contrast to previous implementations based on nonlinear interferometers that necessitate two cascaded SPDCs, thereby substantially simplifying the overall setup. Consequently, this convenient scheme allows us to precisely determine the concentration of the common gases, such as carbon dioxide, by measuring their absorption peaks around 2.7 μm. We also illustrate its broad applicability for detecting various gases by measuring absorption peaks of NH_3 around 3 μm. Furthermore, by carefully reading the spectrum of the near-IR signal photons, the envelope of the CO_2 absorption spectrum can be obtained, indicating its promising prospect for mid-IR spectroscopy. These results present an inexpensive and compact approach to on-chip quantum gas spectroscopy, paving the way for various applications in environmental monitoring/safety, health care, and agriculture.

II. RESULTS AND DISCUSSION

A. Conceptual illustration and theoretical analysis of mid-infrared spectroscopy

The schematic illustration for our quantum sensor is depicted in Fig. 1. A high-quality (Q) factor, Whispering-Gallery Mode (WGM) microcavity with second-order nonlinearity fabricated on a thin-film Lithium Niobate,[53] is coupled with a tapered fiber. A 780 nm pump laser (blue ray in Fig. 1) is launched into the cavity. The spontaneous parametric downconversion with ultra-broadband spectra information can be obtained in such a system, thanks to cavity resonance enhancement. When the phase-matching condition is satisfied, the idler wavelength could even extend into the mid-IR range, which is the absorption fingerprint region for most gas molecules, while the wavelength of the corresponding signal light is kept within the near-IR range. For instance, considering the idler photons around 2.7 μm, which is coincident with the strong absorption peaks of CO_2, the signal wavelength is about 1096 nm, as shown in the inset of Figs. 1(a) and 1(b). According to the inherent quantum correlation[22–25] and coupled-mode theory,[54] there exists a strong correlation between signal and idler photon pairs. Notably, when the cavity is exposed to CO_2 gas, as shown in Fig. 1(a), the evanescent field of the mid-IR idler (yellow) will be absorbed. This will also lead to the annihilation of near-IR signal photons due to their correlation. This could also be understood using a classical model in which the mid-IR absorption introduces an additional loss into the system, which could consequently affect the signal photon generation.

The dynamic of the SPDC in the microcavity can be described by a Hamiltonian,

$$H = \begin{pmatrix} -\Delta_s - i\gamma_s & g a_p \\ -g^* a_p^* & \Delta_i - i\gamma_i - i\kappa_a \end{pmatrix}. \quad (1)$$

Here, we define $\gamma_s = \gamma_{0s} + \gamma_{cs}$ and $\gamma_i = \gamma_{0i} + \gamma_{ci}$, where γ_{0s} and γ_{0i} correspond to the intrinsic decay rate for signal and idler, respectively, caused by material absorption and surface roughness, whereas γ_{cs} and γ_{ci} represent their coupling strength to the single-mode tapered fiber; $\Delta_s = \omega_s - \omega_{0s}$ and $\Delta_i = 2\omega_i - \omega_{0i}$ represent the frequency detuning. g is the nonlinear coupling coefficient for SPDC, which is determined

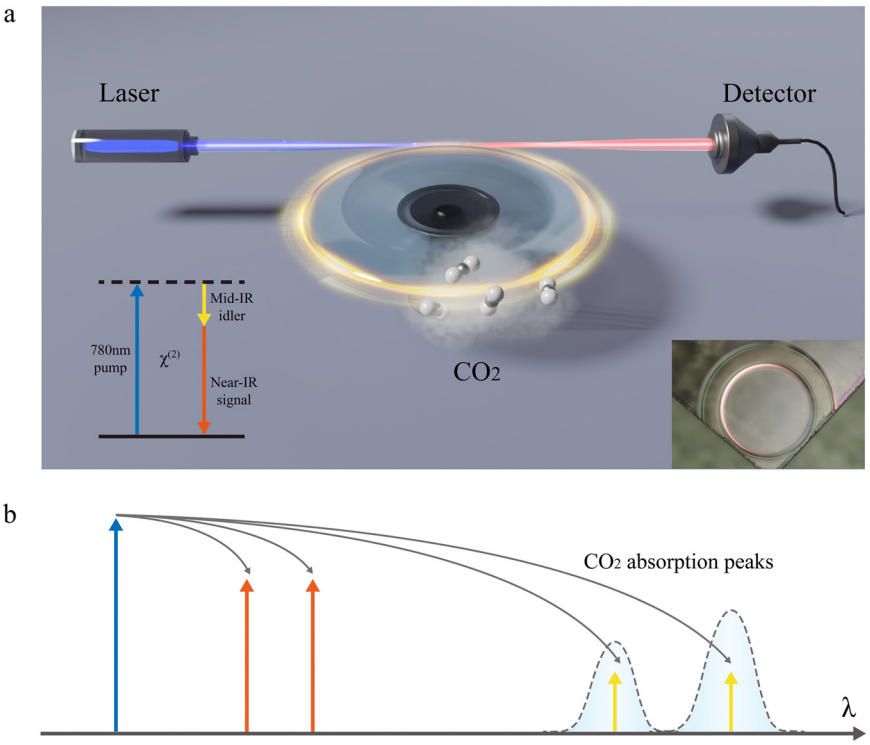

FIG. 1. Conceptual illustration of spectroscopy without mid-infrared photons. (a) Schematic diagram of the device: a tapered fiber is coupled to a microcavity with quadratic nonlinearity. Left inset: the energy level diagram of the SPDC process. Right inset: the top view of the microcavity. (b) The mid-IR idler (yellow) and near-IR signal (red) photon pairs are generated through SPDC when pumped by a 780 nm laser (blue), and the idler wavelength can be adjusted to align with the absorption region (~2.7 μm) of CO_2 gas, which is interacting with the idler evanescent field around the microcavity.

by $\chi^{(2)}$. Under the non-depletion approximation, the pump field a_p is invariant, and ga_p is a constant. In contrast to the traditional SPDC, we have an additional κ_a term in the idler part, which originates from the loss induced by CO_2 absorption. According to the Beer-Lambert law, κ_a is mainly determined by the absorbance of the gas sample and the evanescent field ratio Γ, which is defined as the modal power fraction residing in the air cladding. When this loss term exists, the idler photon field is attenuated and so is the signal field, since they are coupled together by second-order nonlinearity.

With a phase-matching condition, the output signal photon rate R_s can be written as

$$R_s = \frac{2g^2}{\gamma_s + (\gamma_i + \kappa_a)} \frac{\gamma_{cs}\gamma_{cp}}{\gamma_s \gamma_p^2} \frac{P}{\hbar\omega_p}, \tag{2}$$

where P is the input pump power and ω_p is the pump frequency; γ_{cp} is the coupling loss of the pump mode and $\gamma_p = \gamma_{0p} + \gamma_{cp}$ is defined as the total loss for the pump mode. It is clear from the denominator of the first in Eq. (2) that the signal output photon rate R_s is not only determined by the loss of the signal mode itself but also influenced by the loss of its corresponding idler mode. The additional loss rate κ_a induced by the absorption of the idler photons in Eq. (2) will lead to changes in the R_s. Consequently, the CO_2 absorbance, thus the concentration, could be measured by the photon generation rate (PGR) of the near-IR signal light, which could be easily detected by a near-IR detector. Here, the microcavity only serves as an SPDC source and a gas sensor. The mid-IR idler photons are only involved in the sensing/spectroscopy process, transferring information through the coupled-mode equation, but are never measured.

B. Experimental realization of OPO and SPDC in the on-chip microcavity

First, to explore the characteristics of the SPDC, we measure the associated optical parametric oscillation (OPO) spectrum with pump power far exceeding the threshold. The outcoupled light is detected using an optical spectral analyzer shown in Fig. 2(a). It exhibits a broadband output spectrum resembling an optical frequency comb. This arises from the simultaneous satisfaction of phase-matching conditions for many modes in the pump, the signal, and the idler regions, thanks to the dense distribution of WGM modes. No comb lines are recorded at a shorter signal wavelength range of around 1100 nm, whose corresponding idler wavelength is located in the CO_2 absorption region. This can be attributed to a significant phase mismatch between these highly nondegenerate signals (near-IR) and idler modes (mid-IR).

On the other hand, an ultra-broadband SPDC is much easier to achieve. The desired highly nondegenerate photon pairs mentioned earlier can be generated below the threshold. The setup is meticulously designed to measure the generation rate of the signal photons near 1100 nm. The out-coupled light is separated through a 780/1064 wavelength division multiplexer (WDM). The pump light propagating in the 780 nm channel is detected using a photodetector to monitor its coupling status, whereas the near-IR signal light is filtered by a monochromator with a resolution of 1 nm and is probed via a photomultiplier tube (PMT) with a response in the 950–1700 nm band. The signal is also modulated by an optical chopper with a frequency of 10 kHz and is processed by a lock-in amplifier to increase the signal-to-noise ratio. It is unnecessary to consider the coupling and detection for the idler light, as our

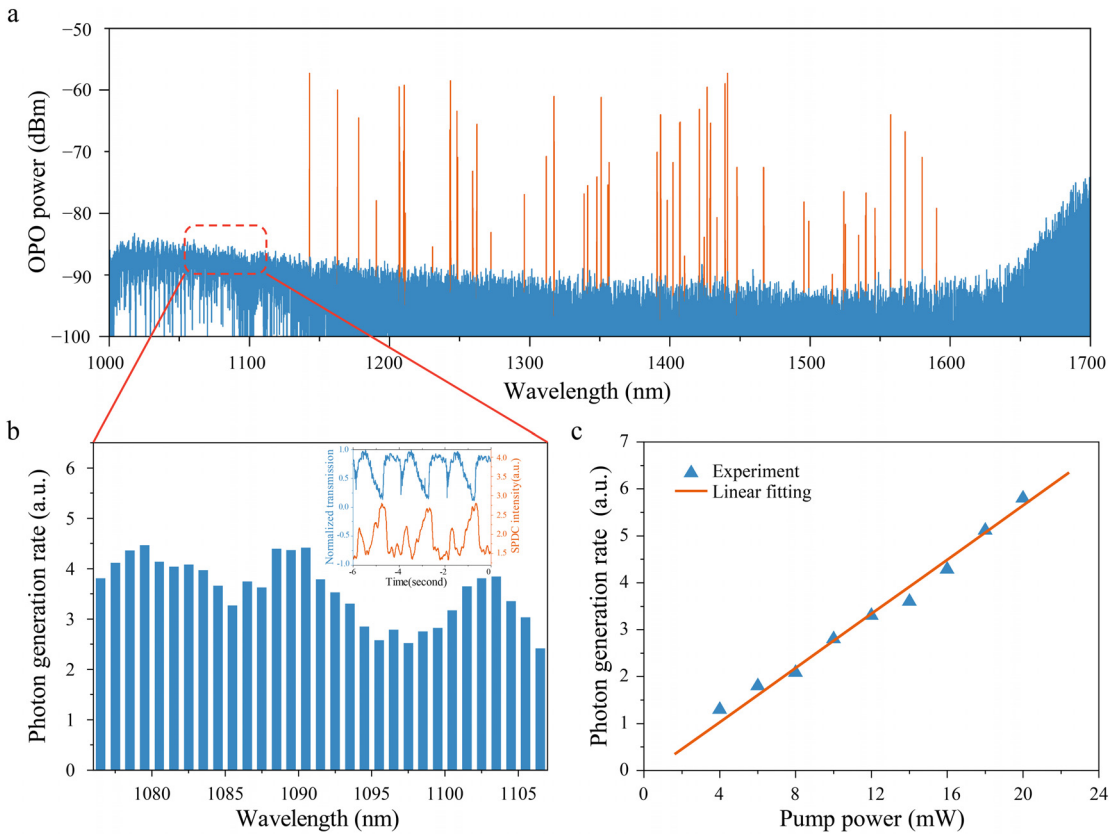

FIG. 2. Experimental observation of optical parametric oscillation and spontaneous downconversion. (a) The recorded comb-like spectrum of the ultra-broadband nondegenerate OPO is shown when the pump power is above the threshold. (b) SPDC spectrum presented by the signal light side from 1076 to 1106 nm with a resolution of 1 nm. Inset: the transmission spectrum of the pump and the signal light. (c) Power dependence of photon generation rate in a wide input pump power range.

method enables gas sensing/spectroscopy without the measurement of mid-IR photons.

The center pump wavelength is tuned to 779.94 nm, corresponding to a high Q ($\sim 10^7$) mode of our cavity. However, $LiNbO_3$ is susceptible to a strong photorefractive (PR) effect. This effect typically features a long response time, which challenges stable laser locking to the WGM resonance and, thus, jeopardizes long-term stability and measurement reliability. Although ultraviolet (UV) irradiation has been reported[55] to mitigate the PR effect and facilitate rapid laser-cavity locking, this method is only effective under moderate PR conditions. In our experiment, the combined effect of the microcavity's high-quality (Q) factor and the relatively high pump power induces a pronounced PR effect, making UV-based compensation inadequate. To circumvent this issue, we instead modulate the laser frequency with a 0.5 Hz triangular wave to scan across the pump resonance. The transmission spectrum of the pump wave and the signal photon counts with a center wavelength of 1096.5 nm are depicted in the inset of Fig. 2(b). The observed linewidth broadening can be attributed to photorefraction. Figure 2(b) illustrates the SPDC spectrum presented by the signal light side in different channels ranging from 1076 to 1106 nm under a pump power of 10.18 mW. The data are obtained by fixing the pump power and recording the peak signal intensity when tuning the center wavelength of the monochromator with 1 nm resolution. Meanwhile, the signal photon in the 1096.5 nm channel is measured at different pump powers, which is demonstrated in Fig. 2(c). A linear dependence of the signal photon generation rate on the pump power can be observed from the result, from which we can verify the spontaneous regime of the parametric process. The result indicates that the photon pairs have ultra-broadband and dense spectral distribution, which paves the way for mid-IR gas sensing/spectroscopy.

C. Mid-IR sensing without mid-IR photons for CO_2

To demonstrate the feasibility of our gas spectroscopy system, we place the microcavity inside a gas chamber, as illustrated in Fig. 3(a), to demonstrate its capability of gas sensing. The pump wavelength, power, and scanning speed are kept consistent with those shown in Fig. 2(b). The inset shows the envelope of the CO_2 absorption spectrum, which is demonstrated through the transmission spectrum R_1/R_0 of signal light across a broad bandwidth. R_1 and R_0 denote the signal photon generation rate with and without the target gas sample, respectively. The realization of gas spectroscopy will be further discussed later. In this context, "on resonance" denotes a scenario where the corresponding idler wavelength of the chosen signal coincides with a strong CO_2 absorption peak, in contrast to "off resonance," where

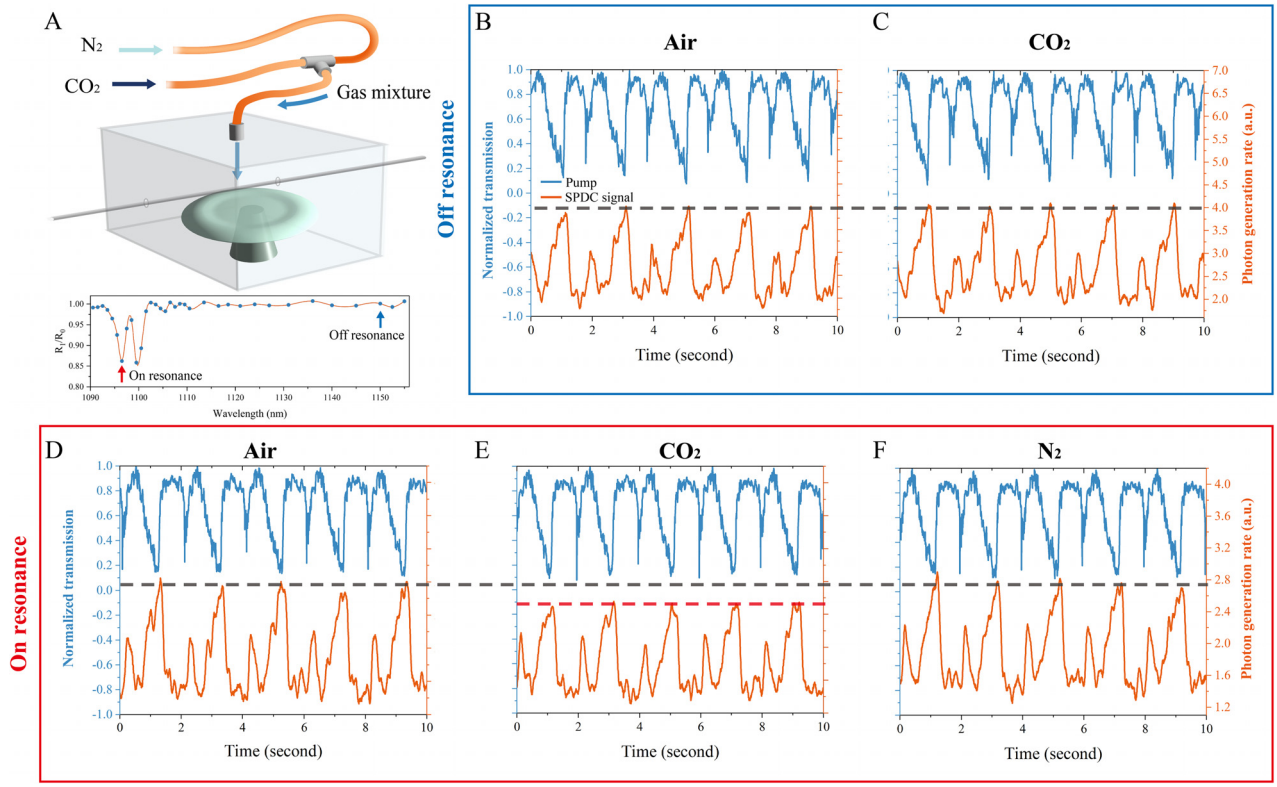

FIG. 3. Quantum gas spectroscopy through SPDC. (a) Schematics of the experimental setup. The gas is injected into a gas cell with an internal microcavity. CO_2 absorption spectrum derived from the broadband transmission measurement of the signal light. On resonance and off resonance indicate whether the idler light wavelength aligns with or is detuned from a CO_2 absorption peak, respectively. (b) and (c) The signal light generation rate when the corresponding idler wavelength is away from the CO_2 absorption region [off resonance marked in (a)], and the transmission of the pump. (d)–(f) The signal spectrum for three types of gas: air, pure CO_2, and pure N_2 when the idler wavelength is coincident with CO_2 absorption near 2.7 μm [on-resonance marked in (a)]. The signal intensity remains invariant under the off resonance situation, only attenuated by the pure CO_2.

the idler wavelength is detuned from any CO_2 absorption features. Initially, we investigate the off resonance scenario where the idler light wavelength is far from the CO_2 absorption region, as shown in Figs. 3(b) and 3(c). By tuning the monochromator to filter signal photons centered at 1150 nm (corresponding to an idler wavelength around 2420 nm), which is a spectral range with negligible CO_2 absorption, we measure the transmission spectrum of pump and signal light without any input gas [Fig. 3(b)]. Subsequently, pure CO_2 gas flow is introduced into the chamber, and its effect on signal photon generation rate is evaluated [Fig. 3(c)]. Remarkably, under this non-absorption condition, no variation in signal photon generation rate occurs, thus excluding potential interference factors such as refraction or temperature changes induced by gas flow.

Next, the signal photons with a center wavelength of 1096.5 nm are filtered for detection. The corresponding idler wavelength is about 2701.6 nm, which coincides with the cluster of strong absorption peaks of CO_2. Figures 3(d)–3(f) depict the transmission spectrum under different gas environments at room temperature and atmospheric pressure: air, pure CO_2, and N_2, respectively. It is observed that the generation rate of signal photons diminishes in the presence of CO_2, while no discernible variation is detected when surrounded by N_2 due to its negligible absorption characteristics. These findings unequivocally demonstrate that any alteration in signal photon counts solely occurs if and only if gas molecules absorb idler photons, thereby affirming both the feasibility and reliability of our system for sensing CO_2 gas. Compared with the previous works based on nonlinear interferometers,[19,23–28] which need two SPDC processes and careful alignment, our method uses only one SPDC process, greatly simplifying measurements. Meanwhile, we use an on-chip microcavity as the device, and the setup is fairly simple, bringing advantages in terms of compactness, stability control, and practical implementation.

Notably, a slight fluctuation of the peak intensity is observed in the signal transmission spectra, probably attributed to the system instability or the mode shift caused by photorefraction. To mitigate the influence of such fluctuations, we measure the photon generation rate over an extended time duration of 500 s and perform curve fitting. Figure 4(a) illustrates the signal photon generation rate, which contains 250 scanning periods. The inset shows CO_2 spectroscopy near 2701.6 nm obtained from the transmission of signal light, which will be discussed in detail in Sec. II D. The signal photons with a center wavelength of 1096.5 nm are filtered for detection, which is marked in the inset, and the corresponding idler wavelength coincides with the absorption peak of CO_2 at 2701.6 nm. The chamber is initially filled with air before the release of the CO_2/N_2 gas mixture [100% CO_2 at

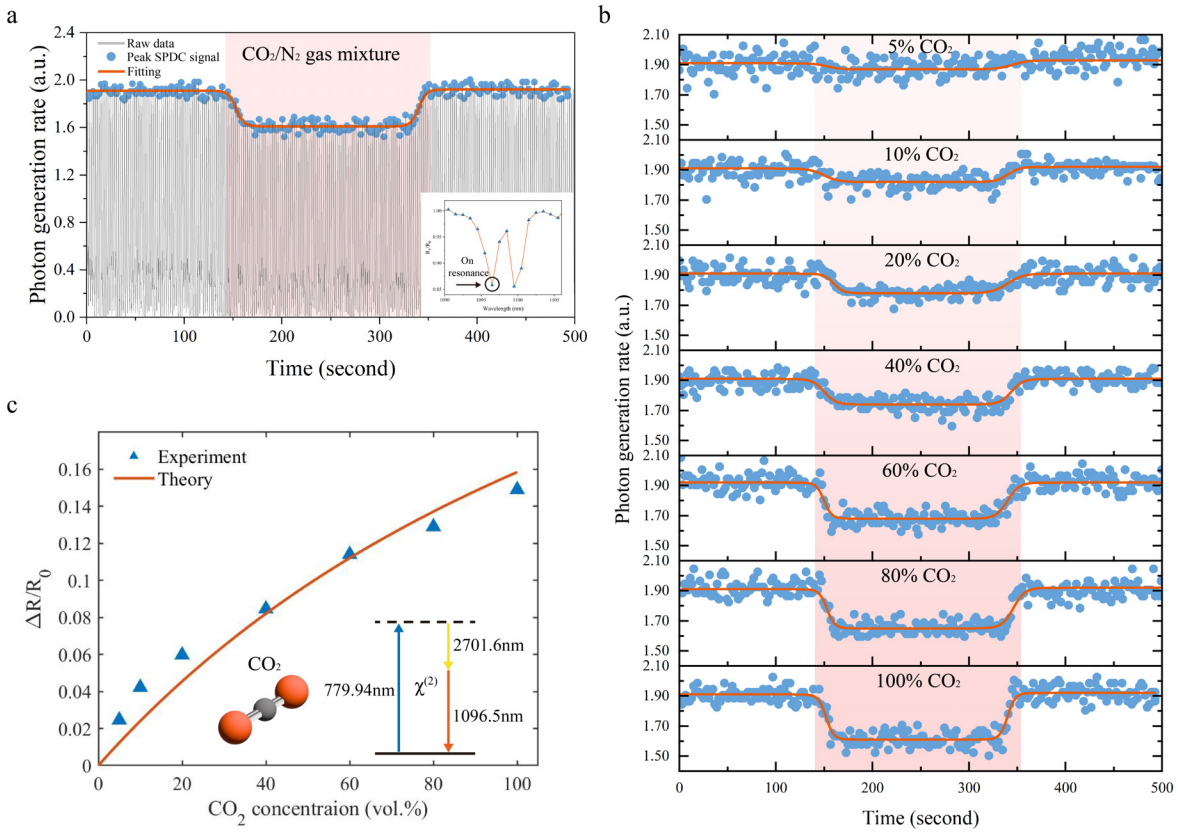

FIG. 4. Gas sensing without mid-IR photons under various CO_2 concentrations. (a) Signal photon generation rate measured over an extended time duration. The gray curves represent the signal transmission spectrum, while the peak intensities during each scan are marked by blue dots. The pink region is when the gas mixture is injected into the cell. Inset: CO_2 spectroscopy near 2701.6 nm obtained from the transmission of signal light. (b) The signal photon generation rate is measured under different CO_2 concentrations. (c) Variations in the photon generation rate as a function of CO_2 concentration. The experiment exhibits a good agreement with the theoretical curve (red). Inset: the schematic diagram for the CO_2 molecule and the energy level diagram of the SPDC process. The pump photon is converted into a signal photon at 1054.1 nm and an idler photon at 2998.9 nm, which is aligned with the absorption peak of CO_2.

atmospheric pressure in Fig. 4(a)]. Afterward, the gas inlet is closed again. The gray curves represent the signal transmission spectrum, with its peak intensity during each pump scanning period indicated by blue dots, and the red curve is the fitting plot. The signal photon generation rate decreases upon the introduction of the gas flow and returns to its initial value after closing the inlet. The absorbance of the gas sample could be derived mathematically once we know the decrement in the signal intensity.

Figure 4(b) illustrates the output signal photon rate measured at different CO_2 concentrations. The data are obtained using the same method mentioned earlier. For 100% CO_2, the variation in the photon generation rate is $\Delta R/R_0 \approx 14.9\%$, where ΔR represents the decrement of the photon rate when the gas sample is released into the chamber. Detecting lower concentrations remains challenging, as the minute variations in photon rate are obscured by signal fluctuations arising from system jitter. The detection limit of our method is approximately 2%, primarily constrained by the quality factors of both the signal and idler modes as well as the evanescent field ratio of the idler mode. The quality factor could be enhanced by an order of magnitude over our current sample through fabrication process improvements. Meanwhile, the limited evanescent field ratio can be mitigated by modifying the mode field distribution, achievable through the use of thinner lithium niobate films or by polishing the edges to form smaller wedge angles. Furthermore, optimizing the optical setup to improve stability and minimize system jitter would reduce signal fluctuations and enhance the signal-to-noise ratio. The $\Delta R/R_0$ is plotted as a function of CO_2 concentration in Fig. 4(c). The experimental result shows a good agreement with the theoretical prediction (see the supplementary material). Our method is convenient and cost-effective by using a compact system free of a mid-IR source and detector. The measurement can be completed without a mid-IR source or detector in that we can derive the gas concentration directly from $\Delta R/R_0$ of the near-IR signal photons.

D. CO_2 spectroscopy without mid-IR photons

Our method has shown satisfactory performance and unique advantages in mid-IR sensing. However, gas spectroscopy, which can reveal specific and detailed spectral information, is also highly desired for both scientific research and industrial applications. Due to the limited resolution of our monochromator, it is impossible to resolve every single absorption peak in our experiment. However, the envelope of

CO_2 absorption spectra can be obtained. Some of the spectroscopic information of CO_2 has already been demonstrated in Figs. 3 and 4. The experimental setup is illustrated in Fig. 5(a). We tune the center wavelength of the monochromator step by step from 1076 to 1106 nm with a resolution of 1 nm and measure the absorption strength $\Delta R/R_0$ for 100% CO_2 at each step using the same method as mentioned before. The experimental result demonstrated in Fig. 5(c) outlines the envelope of the cluster of CO_2 absorption bands near 2.7 μm, which matches well with the absorption spectrum retrieved from the HITRAN databases.[56] If the resolution of the monochromator is high enough, it is possible for us to achieve detailed spectroscopic information by scanning one SPDC peak across the absorption lines through temperature tuning of the cavity.

E. Mid-IR sensing without mid-IR photons for NH_3

Notably, our method exhibits broad applicability for detecting any gas exhibiting strong mid-infrared absorption. This represents a significant breakthrough, as conventional mid-infrared gas detection techniques typically require distinct light sources for different target gases due to significant variations in their absorption wavelengths, preventing a single apparatus from accommodating multiple analytes. In contrast, our approach eliminates the need for source replacement. Detection across different gases is achieved using the same system merely by selecting appropriate signal light wavelengths. This significantly enhances operational accessibility and system versatility.

To demonstrate its applicability to the detection of various gases, in addition to the carbon dioxide results presented earlier, we experimentally demonstrated the detection of ammonia concentration. We change the center wavelength of the monochromator to 1053.9 nm to choose another signal photon for detection. The corresponding idler wavelength is about 2998.9 nm, which is aligned with the absorption peak of NH_3. As shown in Fig. 6(a), the photon generation rate is monitored over an extended duration. The chamber is initially purged with N_2, followed by the introduction of an NH_3/N_2 gas mixture and subsequently purged again with N_2. The inset shows the NH_3 absorption spectrum near 2998.9 nm. Figure 6(b) demonstrates the signal photon rates measured at varying NH_3 concentrations. Gas concentrations are derived directly from $\Delta R/R_0$ using the established methodology, as is shown in Fig. 6(c). This experimental procedure and resultant data are analogous to the CO_2 case, confirming the system's capability for multi-gas molecular detection. Furthermore, our method enables simultaneous detection of multiple distinct gases within a single experiment, provided their absorption wavelengths differ. For instance, differing mid-infrared absorption wavelengths of CO_2 and NH_3 allow their respective concentrations to be determined concurrently. This can be achieved by simultaneously measuring the signal photon counts at their corresponding wavelengths, without requiring system reconfiguration or source adjustment, thereby offering a highly efficient and streamlined approach.

III. CONCLUSION

In summary, we have successfully demonstrated a microcavity-based quantum gas sensor capable of mid-IR gas spectroscopy without the need for mid-IR photons, utilizing quantum correlation in SPDC.

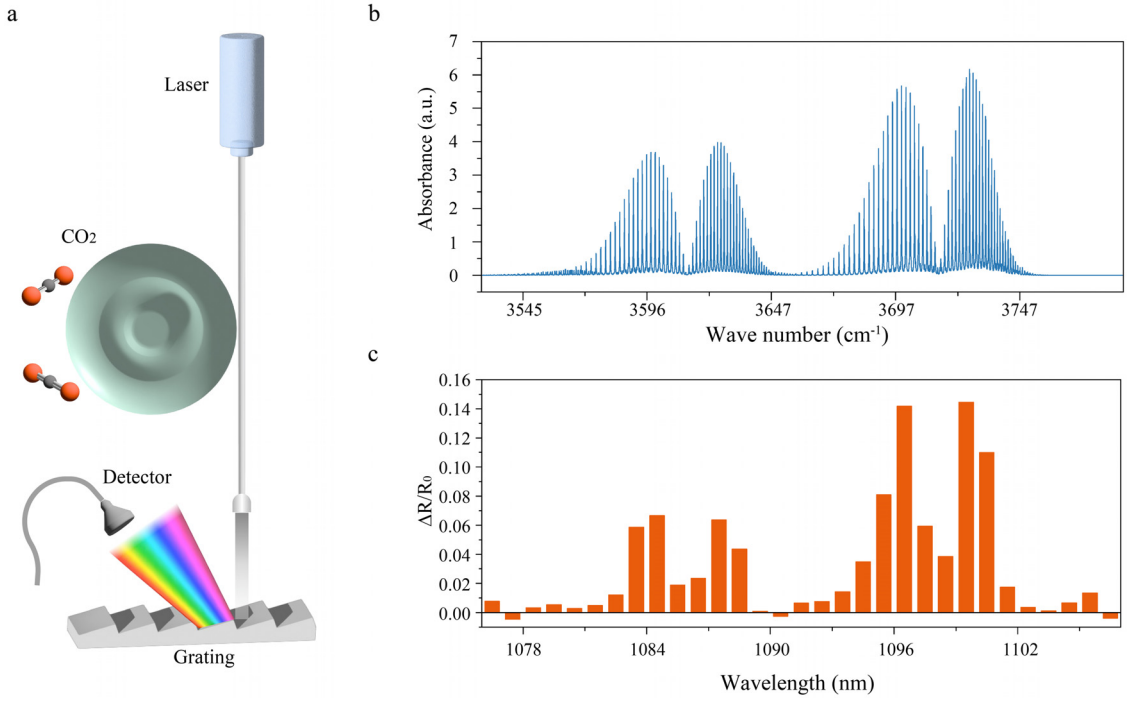

FIG. 5. CO_2 spectroscopy without mid-IR photons. (a) Schematics of the experimental setup. The signal photons are filtered via a monochromator and detected by the PMT. (b) CO_2 absorption spectrum near 2.7 μm retrieved from the HITRAN databases.[56] (c) $\Delta R/R_0$ obtained at 100% CO_2 concentration. The data are measured sequentially from 1076 to 1106 nm with a resolution of 1 nm.

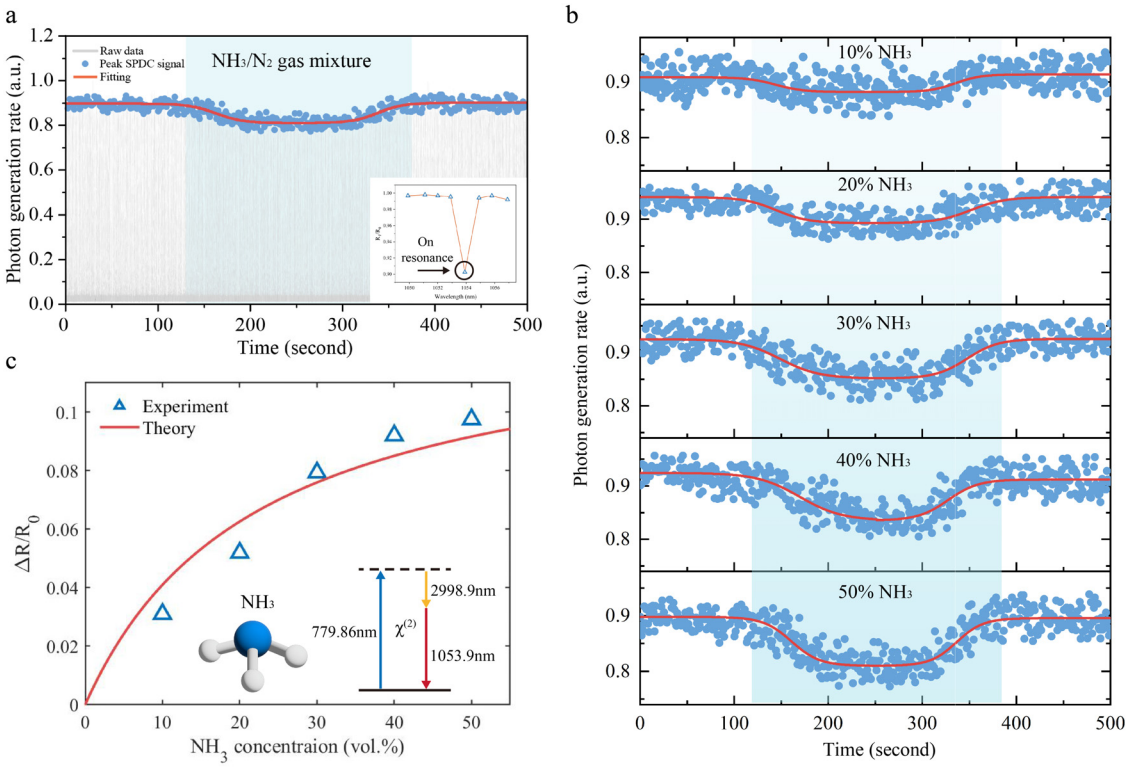

FIG. 6. Gas sensing without mid-IR photons for NH_3 with different concentrations. (a) Signal photon generation rate measured over an extended time duration via the same method as in Fig. 4. The blue region is when the NH_3/N_2 gas mixture is injected into the cell. Inset: NH_3 spectroscopy near 2998.9 nm obtained from the transmission of signal light. (b) The signal photon generation rate is measured under different NH_3 concentrations. (c) Variations in the photon generation rate as a function of concentration. Inset: the schematic diagram for the NH_3 molecule and the energy level diagram of the SPDC process. The pump photon is converted into a signal photon at 1053.9 nm and an idler photon at 2998.9 nm, which is aligned with the absorption peak of NH_3.

Our approach eliminates the requirement for mid-IR optical components and does not necessarily involve the generation or detection of mid-IR photons throughout the process, as the gas concentration can be directly inferred from the near-IR signal photon generation rate. Compared to previous studies,[22,26] our scheme employs a single SPDC process and an on-chip microcavity, offering significant advantages in terms of compactness, cost-effectiveness, and operational convenience. Meanwhile, detection across different gases can be achieved using the same system without the need for source replacement merely by selecting different signal photon wavelengths, which significantly enhances operational accessibility and system versatility. Furthermore, by carefully analyzing the spectrum of near-IR idler photons, we can obtain information about the envelope of the CO_2 absorption spectrum, highlighting its promising potential for mid-IR spectroscopy. These findings present an economical and compact on-chip approach to quantum gas sensing/spectroscopy that paves the way for various applications ranging from environmental monitoring/safety to agriculture and medical healthcare.

IV. MATERIALS AND METHODS

A. Optical parametric oscillation and spontaneous downconversion

Our experimental platform is based on a thin-film lithium niobate microdisk resonant cavity, whose diameter is approximately 1 mm and thickness is about 3 μm. A narrow linewidth laser (CTL, Toptica Photonics) operating at 1560 nm is utilized as the seed for the second harmonic generator (VENUS, Connet Laser Technology Co., LTD), which incorporates a PPLN crystal to generate light around 780 nm. The coupling of this 780 nm pump light into the microcavity is achieved through a tapered fiber, with precise control over the coupling status accomplished by adjusting the gap between the microcavity and fiber using a 3-axis nano-translation stage (MDT630B, Thorlabs). The pump wavelength is set to scan around 779.94 nm using a 0.5 Hz triangular wave, which launches a WGM with a quality factor as high as 10^7. For OPO measurement, a spectrum analyzer (Agilent, E4440A) is connected to the other side of the tapered fiber to observe the out-coupled spectrum. For SPDC, the out-coupled light is divided through a 780/1064 wavelength division multiplexer (WDM). The transmission spectrum of the 780 nm pump light is monitored using a Si-based photodetector (DET10A/M, Thorlabs), whereas the near-IR signal light in the 1064 nm channel is filtered by a hand-made monochromator consisting of a grating (GR25-0610, Thorlabs), whose resolution is approximately 1 nm. The filtered photons are probed via a photomultiplier tube (PMT) with a response in the 950–1700 nm band (H10330A-75, Hamamatsu). The signal is also modulated by an optical chopper (SYSU scientific instruments) with a frequency of 10 kHz and is processed by a lock-in amplifier (SR865A, Stanford Research Systems) to increase the signal-to-noise ratio, detecting the weak signal embedded in high background noise.

B. Gas sensing and spectroscopy

In the sensing process, we tune the monochromator to filter signal photons centered at 1096.5 nm, which corresponds to an idler wavelength around 2420 nm. The CO_2 has strong absorption resonances in this region. We measure the signal transmission spectra under different gas environments at room temperature and atmospheric pressure and compare their signal photon generation rate. We also change the concentration of CO_2 in the gas mixture and repeat the experiment to investigate its impact on the signal photon generation rate. The spectroscopy experiment is done by repeating this procedure when changing the center wavelength of the monochromator step by step from 1076 to 1106 nm with a resolution of 1 nm and recording the $\Delta R/R_0$.

C. Sample fabrication

The microdisk utilized in our experiment possesses a diameter of approximately 1 mm and a thickness of about 3 μm, exhibiting an exceptional quality factor reaching 10^7. This microcavity is fabricated on a lithium niobate on insulator (LNOI) chip through the utilization of photolithography-assisted chemo-mechanical etching (PLACE). Initially, a protective layer composed of chromium with a thickness of around 600 nm is deposited onto the surface of the meticulously cleaned lithium niobate film for polishing purpose. Subsequently, photolithography technology combined with wet etching techniques is employed to achieve desired patterns within the chromium layer situated atop the lithium niobate film. Following this step, chemical mechanical polishing (CMP) is performed to polish the sample, resulting in the formation of a smooth-walled microdisk structure. The final stages involve removing the chromium layer from the lithium niobate microdisk using wet etching and transforming the underlying silicon dioxide into pillar structures via hydrofluoric acid etching. Ultimately, we successfully obtain a suspended lithium niobate on insulator (LNOI) microdisk structure.

SUPPLEMENTARY MATERIAL

See the supplementary material for additional information about the experimental methods and a detailed discussion of the numerical simulations.

ACKNOWLEDGMENTS

This work was supported by the National Science Foundation of China (Grant Nos. 12274295, 12334014, and 12192251), the National Key Research and Development Program (Nos. 2023YFA1407200 and 2023YFB3906400), and the Shanghai Technology Innovation Project (Grant No. 24590711300).

AUTHOR DECLARATIONS

Conflict of Interest

The authors have no conflicts to disclose.

Author Contributions

Boyi Xue and Renhong Gao contributed equally to this work.

Boyi Xue: Data curation (lead); Investigation (lead); Validation (lead); Visualization (lead); Writing – original draft (lead). **Renhong Gao:** Resources (lead). **Yicheng Zhu:** Investigation (supporting). **Hengzhe Yan:** Investigation (supporting); Methodology (supporting). **Jiankun Hou:** Investigation (supporting). **Xianfeng Chen:** Supervision (equal). **Ya Cheng:** Supervision (equal). **Jintian Lin:** Resources (equal); Supervision (equal). **Li Ge:** Supervision (equal). **Wenjie Wan:** Conceptualization (equal); Funding acquisition (equal); Methodology (equal); Project administration (equal); Supervision (equal); Writing – review & editing (equal).

DATA AVAILABILITY

The data that support the findings of this study are available from the corresponding authors upon reasonable request.

REFERENCES

[1]B. Hinkov, F. Pilat, L. Lux, P. L. Souza, M. David, A. Schwaighofer, D. Ristanić, B. Schwarz, H. Detz, A. M. Andrews, B. Lendl, and G. Strasser, "A mid-infrared lab-on-a-chip for dynamic reaction monitoring," Nat. Commun. **13**(1), 4753 (2022).
[2]M. C. Estevez, M. Alvarez, and L. M. Lechuga, "Integrated optical devices for lab-on-a-chip biosensing applications," Laser Photonics Rev. **6**, 463–487 (2012).
[3]Y. Chen, H. Lin, J. Hu, and M. Li, "Heterogeneously integrated silicon photonics for the mid-infrared and spectroscopic sensing," ACS Nano **8**, 6955–6961 (2014).
[4]I. Pupeza, M. Huber, M. Trubetskov *et al.*, "Field-resolved infrared spectroscopy of biological systems," Nature **577**, 52–59 (2020).
[5]J. Seo, S. Warnke, K. Pagel, M. T. Bowers, and G. von Helden, "Infrared spectrum and structure of the homochiral serine octamer–dichloride complex," Nat. Chem. **9**, 1263 (2017).
[6]K. R. Asmis, N. L. Pivonka, G. Santambrogio, M. Brümmer, C. Kaposta, D. M. Neumark, and L. Wöste, "Gas-phase infrared spectrum of the protonated water dimer," Science **299**, 1375 (2003).
[7]J. M. Headrick, E. G. Diken, R. S. Walters, N. I. Hammer, R. A. Christie, J. Cui, E. M. Myshakin, M. A. Duncan, M. A. Johnson, and K. D. Jordan, "Spectral signatures of hydrated proton vibrations in water clusters," Science **308**, 1765 (2005).
[8]W. Miekisch, J. K. Schubert, and G. F. E. Noeldge-Schomburg, "Diagnostic potential of breath analysis–focus on volatile organic compounds," Clin. Chim. Acta **347**(1–2), 25–39 (2004).
[9]L. Tombez, E. J. Zhang, J. S. Orcutt, S. Kamlapurkar, and W. M. J. Green, "Methane absorption spectroscopy on a silicon photonic chip," Optica **4**, 1322–1325 (2017).
[10]U. Willer, M. Saraji, A. Khorsandi, P. Geiser, and W. Schade, "Near- and mid-infrared laser monitoring of industrial processes, environment and security applications," Opt. Lasers Eng. **44**, 699–710 (2006).
[11]A. Chatterjee, M. M. Gierach, A. J. Sutton, R. A. Feely, D. Crisp, A. Eldering, M. R. Gunson, C. W. O'Dell, B. B. Stephens, and D. S. Schimel, "Influence of El Niño on atmospheric CO_2 over the tropical Pacific Ocean: Findings from NASA's OCO-2 mission," Science **358**(6360), eaam5776 (2017).
[12]E.-M. Metz, S. N. Vardag, S. Basu, M. Jung, B. Ahrens, T. El-Madany, S. Sitch, V. K. Arora, P. R. Briggs, and P. Friedlingstein, "Soil respiration-driven CO_2 pulses dominate Australia's flux variability," Science **379**, 1332–1335 (2023).
[13]D. M. Kita, B. Miranda, D. Favela, D. Bono, J. Michon, H. Lin, T. Gu, and J. Hu, "High-performance and scalable on-chip digital Fourier transform spectroscopy," Nat. Commun. **9**, 4405 (2018).
[14]Q. Du, Z. Luo, H. Zhong, Y. Zhang, Y. Huang, T. Du, W. Zhang, T. Gu, and J. Hu, "Chip-scale broadband spectroscopic chemical sensing using an integrated supercontinuum source in a chalcogenide glass waveguide," Photonics Res. **6**, 506–510 (2018).
[15]A. Rogalski, "Infrared detectors: An overview," Infrared Phys. Technol. **43**, 187–210 (2002).
[16]A. Godard, "Infrared (2-12 μm) solid-state laser sources: A review," C. R. Phys. **8**(10), 1100–1128 (2007).

[17]A. P. Ravikumar, J. De Jesus, M. C. Tamargo, and C. F. Gmachl, "High performance, room temperature, broadband II–VI quantum cascade detector," Appl. Phys. Lett. **107**(14), 141105 (2015).
[18]Y. Yao, A. J. Hoffman, and C. F. Gmachl, "Mid-infrared quantum cascade lasers," Nat. Photonics **6**(7), 432–439 (2012).
[19]Z. Liu, D. Wasserman, S. S. Howard, A. J. Hoffman, C. F. Gmachl, X. Wang, T. Tanbun-Ek, L. Cheng, and F.-S. Choa, "Room-temperature continuous-wave quantum cascade lasers grown by MOCVD without lateral Regrowth," IEEE Photonics Technol. Lett. **18**(12), 1347–1349 (2006).
[20]A. H. Atabaki, S. Moazeni, F. Pavanello, H. Gevorgyan, J. Notaros, L. Alloatti, M. T. Wade, C. Sun, S. A. Kruger, H. Meng, K. Al Qubaisi, I. Wang, B. Zhang, A. Khilo, C. V. Baiocco, M. A. Popović, V. M. Stojanović, and R. J. Ram, "Integrating photonics with silicon nanoelectronics for the next generation of systems on a chip," Nature **556**, 349–354 (2018).
[21]H. Lin, Z. Luo, T. Gu, L. Kimerling, K. Wada, A. Agarwal, and J. Hu, "Mid-infrared integrated photonics on silicon: A perspective," Nanophotonics **7**, 393–420 (2017).
[22]G. B. Lemos, V. Borish, G. D. Cole, S. Ramelow, R. Lapkiewicz, and A. Zeilinger, "Quantum imaging with undetected photons," Nature **512**, 409–412 (2014).
[23]L. Wang, X. Zou, and L. Mandel, "Induced coherence without induced emission," Phys. Rev. A **44**, 4614–4622 (1991).
[24]X. Zou, L. Wang, and L. Mandel, "Induced coherence and indistinguishability in optical interference," Phys. Rev. Lett. **67**, 318–321 (1991).
[25]L. Mandel, "Quantum effects in one-photon and two-photon interference," Rev. Mod. Phys. **71**, S274–S282 (1999).
[26]D. A. Kalashnikov, A. V. Paterova, S. P. Kulik, and L. A. Krivitsky, "Infrared spectroscopy with visible light," Nat. Photonics **10**, 98–101 (2016).
[27]A. Paterova, H. Yang, C. An, D. Kalashnikov, and L. Krivitsky, "Measurement of infrared optical constants with visible photons," New J. Phys. **20**, 043015 (2018).
[28]A. V. Paterova, H. Yang, C. An, D. A. Kalashnikov, and L. A. Krivitsky, "Tunable optical coherence tomography in the infrared range using visible photons," Quantum Sci. Technol. **3**, 025008 (2018).
[29]A. Vanselow, P. Kaufmann, I. Zorin, B. Heise, H. M. Chrzanowski, and S. Ramelow, "Frequency-domain optical coherence tomography with undetected mid-infrared photons," Optica **7**(12), 1729 (2020).
[30]A. V. Paterova, S. M. Maniam, H. Yang, G. Grenci, and L. A. Krivitsky, "Hyperspectral infrared microscopy with visible light," Sci. Adv. **6**, eabd0460 (2020).
[31]I. Kviatkovsky, H. M. Chrzanowski, E. G. Avery, H. Bartolomaeus, and S. Ramelow, "Microscopy with undetected photons in the mid-infrared," Sci. Adv. **6**, eabd0264 (2020).
[32]X. Jiang, A. J. Qavi, S. H. Huang, and L. Yang, "Whispering-gallery sensors," Matter **3**, 371–392 (2020).
[33]M. R. Foreman, J. D. Swaim, and F. Vollmer, "Whispering gallery mode sensors," Adv. Opt. Photonics **7**, 168–240 (2015).
[34]L. Xu, X. Jiang, G. Zhao, D. Ma, H. Tao, Z. Liu, F. G. Omenetto, and L. Yang, "High-Q silk fibroin whispering gallery microresonator," Opt. Express **24**, 20825–20830 (2016).
[35]B.-B. Li, W. R. Clements, X.-C. Yu, K. Shi, Q. Gong, and Y.-F. Xiao, "Single nanoparticle detection using split-mode microcavity Raman lasers," Proc. Natl. Acad. Sci. U. S. A. **111**, 14657–14662 (2014).
[36]B. Q. Shen, X. C. Yu, Y. Zhi, L. Wang, D. Kim, Q. Gong, and Y. F. Xiao, "Detection of single nanoparticles using the dissipative interaction in a high-Q microcavity," Phys. Rev. Appl. **5**, 024011 (2016).
[37]F. Vollmer, D. Braun, A. Libchaber, M. Khoshsima, I. Teraoka, and S. Arnold, "Protein detection by optical shift of a resonant microcavity," Appl. Phys. Lett. **80**, 4057–4059 (2002).
[38]S. Rosenblum, Y. Lovsky, L. Arazi, F. Vollmer, and B. Dayan, "Cavity ring-up spectroscopy for ultrafast sensing with optical microresonators," Nat. Commun. **6**, 6788 (2015).
[39]M. D. Baaske and F. Vollmer, "Optical observation of single atomic ions interacting with plasmonic nanorods in aqueous solution," Nat. Photonics **10**, 733–739 (2016).
[40]Y. Zhi, X. Yu, H. Chen, B. Guan, and Y.-F. Xiao, "Noise suppression of mechanical oscillations in a microcavity for ultrasensitive detection," Opt. Lett. **44**, 2426–2429 (2019).
[41]Y. Y. Li, Q. T. Cao, J. H. Chen, X. C. Yu, and Y. F. Xiao, "Microcavity sensor enhanced by spontaneous chiral symmetry breaking," Phys. Rev. Appl. **16**, 044016 (2021).
[42]X.-C. Yu, S.-J. Tang, W. Liu, Y. Xu, Q. Gong, Y.-L. Chen, and Y.-F. Xiao, "Single-molecule optofluidic microsensor with interface whispering gallery modes," Proc. Natl. Acad. Sci. U. S. A. **119**, e2108678119 (2022).
[43]Y. Zhi, X.-C. Yu, Q. Gong, L. Yang, and Y.-F. Xiao, "Single nanoparticle detection using optical microcavities," Adv. Mater. **29**, 1604920 (2017).
[44]Y. Hu, L. Shao, S. Arnold, Y.-C. Liu, C.-Y. Ma, and Y.-F. Xiao, "Mode broadening induced by nanoparticles in an optical whispering-gallery microcavity," Phys. Rev. A **90**, 043847 (2014).
[45]M. Loyez, M. Adolphson, J. Liao *et al.*, "From whispering gallery mode resonators to biochemical sensors," ACS Sens. **8**, 2440–2470 (2023).
[46]M. E. Anderson, E. C. O'Brien, E. N. Grayek, J. K. Hermansen, and H. K. Hunt, "The detection of helicobacter hepaticus using whispering-gallery mode microcavity optical sensors," Biosensors **5**, 562–576 (2015).
[47]M. S. McClellan, L. L. Domier, and R. C. Bailey, "Label-free virus detection using silicon photonic microring resonators," Biosens. Bioelectron. **31**, 388–392 (2012).
[48]S.-J. Tang, M. Zhang, J. Sun, J.-W. Meng, X. Xiong, Q. Gong, D. Jin, Q.-F. Yang, and Y.-F. Xiao, "Single-particle photoacoustic vibrational spectroscopy using optical microresonators," Nat. Photonics **17**, 951 (2023).
[49]W. Liu, Y.-L. Chen, S.-J. Tang, F. Vollmer, and Y.-F. Xiao, "Nonlinear sensing with whispering-gallery mode microcavities: From label-free detection to spectral fingerprinting," Nano Lett. **21**, 1566–1575 (2021).
[50]J. Liao and L. Yang, "Optical whispering-gallery mode barcodes for high-precision and wide-range temperature measurements," Light: Sci. Appl. **10**, 32 (2021).
[51]E. Gavartin, P. Verlot, and T. J. Kippenberg, "A hybrid on-chip optomechanical transducer for ultrasensitive force measurements," Nat. Nanotechnol. **7**, 509 (2012).
[52]F. Ottonello-Briano, C. Errando-Herranz, H. Rödjegård, H. Martin, H. Sohlström, and K. Gylfason, "Carbon dioxide absorption spectroscopy with a mid-infrared silicon photonic waveguide," Opt. Lett. **45**, 109–112 (2020).
[53]R. Gao, H. Zhang, F. Bo, W. Fang, Z. Hao, N. Yao, J. Lin, J. Guan, L. Deng, M. Wang, L. Qiao, and Y. Cheng, "Broadband highly efficient nonlinear optical processes in on-chip integrated lithium niobate microdisk resonators of Q-factor above 108," New J. Phys. **23**, 123027 (2021).
[54]X. Guo, C.-L. Zou, C. Schuck, H. Jung, R. Cheng, and H. X. Tang, "Parametric down-conversion photon-pair source on a nanophotonic chip," Light: Sci. Appl. **6**, e16249 (2016).
[55]J. Hou, B. Xue, R. Ma, S. Yu, Y. Zhu, X. Chen, J. Lu, and W. Wan, "UV-enhanced photorefractive response rate in a thin-film lithium niobate microdisk," Opt. Lett. **49**, 3456 (2024).
[56]I. E. Gordon, L. S. Rothman, R. J. Hargreaves, R. Hashemi, E. V. Karlovets, F. M. Skinner *et al.*, "The HITRAN2020 molecular spectroscopic database," J. Quant. Spectrosc. Radiat. Transfer **277**, 107949 (2022).